APPLIED SCIENCES AND ENGINEERING

One-step rolling fabrication of VO_2 tubular bolometers with polarization-sensitive and omnidirectional detection

Binmin Wu[1,2,3], Ziyu Zhang[1,2,3], Bingxin Chen[4], Zhi Zheng[1,2,3], Chunyu You[1,2,3], Chang Liu[1,2,3], Xing Li[1,2,3], Jinlong Wang[1,2,3], Yunqi Wang[1,2,3], Enming Song[3,5], Jizhai Cui[1,2,3], Zhenghua An[4], Gaoshan Huang[1,2,3], Yongfeng Mei[1,2,3,5]*

Uncooled infrared detection based on vanadium dioxide (VO_2) radiometer is highly demanded in temperature monitoring and security protection. The key to its breakthrough is to fabricate bolometer arrays with great absorbance and excellent thermal insulation using a straightforward procedure. Here, we show a tubular bolometer by one-step rolling VO_2 nanomembranes with enhanced infrared detection. The tubular geometry enhances the thermal insulation, light absorption, and temperature sensitivity of freestanding VO_2 nanomembranes. This tubular VO_2 bolometer exhibits a detectivity of ~2×10^8 cm $Hz^{1/2}$ W^{-1} in the ultrabroad infrared spectrum, a response time of ~2.0 ms, and a calculated noise-equivalent temperature difference of 64.5 mK. Furthermore, our device presents a workable structural paradigm for polarization-sensitive and omnidirectional light coupling bolometers. The demonstrated overall characteristics suggest that tubular bolometers have the potential to narrow performance and cost gap between photon detectors and thermal detectors with low cost and broad applications.

INTRODUCTION

Infrared photodetectors are widely applied in our daily life, such as remote thermometer (*1*, *2*), environmental monitoring (*3*, *4*), and personal search and rescue in geological disasters (*5*, *6*). Uncooled infrared detection technology is increasingly being developed to meet the portability of daily monitoring and the capability for various application scenarios. To achieve high sensitivity and intensity, uncooled infrared detectors comprise a heat-sensitive suspended layer or structure on a wafer with excellent thermal insulation and enhanced signal collection (*7*). Advances in microfabrication technology have enabled the manufacture of uncooled infrared thermal detectors with various structures such as cantilever (*8*, *9*) and antennas (*10*, *11*), in addition to the established pellicle-supported and microbridge structures. Uncooled focal plane arrays based on bolometers, pyroelectric detectors, and thermopiles have reached a noise-equivalent temperature difference (NETD) of less than 0.1 K (*12*), which have been implemented in the night vision systems and infrared cameras. A bolometer based on polycrystalline vanadium oxide nanomembrane (*13*–*15*) is achieved with high temperature coefficient of resistance (TCR) and good processability for uncooled thermal imaging devices (*16*). However, complicated structures to improve the thermal insulation and signal enhancement require a multiple-step process in the microfabrication (*17*–*19*), which thus increases system complexity and manufacturing cost with low yield (*20*, *21*). Furthermore, the portable polarimetry and wide-angle infrared imaging system, which operates without the need for lenses, offers advantages and extensive application opportunities in identifying detection targets amidst complicated environments such as smoke, haze, and camouflage. However, its production presents challenges.

Here, we report a sensitive tubular vanadium dioxide (VO_2) bolometer fabricated by one-step rolling for polarization-sensitive and omnidirectional infrared detection. Rolled-up nanomembrane technology can be combined with existing chip fabrication methods to convert specified VO_2 precursor planar nanomembranes into microtubes with three-dimensional (3D) geometries. Theoretical simulation and experimental verification prove that tubular geometry can provide superior thermal insulation and trap infrared light. The atomic structure of the rolled-up VO_2 nanomembrane was investigated by in situ temperature-variable transmission electron microscopy (TEM), with compressive strain that reduces the phase transition temperature from 68° to 40°C. This tubular VO_2 bolometer exhibits a detectivity of ~2×10^8 cm $Hz^{1/2}$ W^{-1}, a response time of ~2.0 ms, and a calculated NETD of 64.6 mK over a broad infrared spectrum. Besides, the VO_2 bolometer with tubular geometry can offer polarization-sensitive and omnidirectional detection under a wide incident angle of 150°, which brings vitality to the development of uncooled infrared focal plane technology. More profoundly, our tubular bolometers offer a promising integration platform for photon/electron chips by forming 3D volumetric devices with a more compact footprint.

[1]Department of Materials Science & State Key Laboratory of ASIC and Systems, Fudan University, Shanghai 200438, People's Republic of China. [2]Yiwu Research Institute of Fudan University, Yiwu, Zhejiang 322000, People's Republic of China. [3]International Institute of Intelligent Nanorobots and Nanosystems, Fudan University, Shanghai 200438, People's Republic of China. [4]State Key Laboratory of Surface Physics and Institute for Nanoelectronic Devices and Quantum Computing, Department of Physics, Fudan University, Shanghai 200438, People's Republic of China. [5]Shanghai Frontiers Science Research Base of Intelligent Optoelectronics and Perception, Institute of Optoelectronics, Fudan University, Shanghai 200438, People's Republic of China.
*Corresponding author. Email: yfm@fudan.edu.cn

RESULTS

Design methodology of rolled-up tubular bolometers

The structure of the bolometer is directly related to the thermal insulation and light absorption of the nanomembranes. As a typical 3D structure, the tube consists of uniform walls and cylindrical cavities. In an ideal case, the contact between the tube and the plane is a line, which can greatly reduce the direct heat transfer between tube and plane so that a tubular device with high thermal insulation can be realized by occupying much smaller area on the chip. Moreover, the tubular microcavity structure is a typical and effective light trap structure, which can effectively enhance the interaction between the light and the tube wall and improve the absorption of incident rays. Figure 1A schematically depicts the structure of an on-chip tubular bolometer with a thermal sensitive nanomembrane and metal electrodes. The sensitive nanomembrane (i.e., VO_2 nanomembrane in present case) becomes hotter (ΔT) when exposed to infrared light, which causes a resistance drop (ΔR) that can be detected by the circuit (ΔI). The corresponding fabrication process is shown in Fig. 1B. Briefly, VO_2/Cr bilayer with strain gradient was grown on silicon wafer with silicon dioxide (SiO_2) sacrificial layer. After the removal of SiO_2 layer, VO_2/Cr bilayer is detached from the substrate and rolled up because of the strain gradient. Figure 1C shows a 3×4 array of the fabricated VO_2/Cr microtubes. To further demonstrate the thermal insulation and optical coupling mechanism of the tubular bolometer, the thermal distribution in the thermal radiation field and the electromagnetic wave distribution of the optical field were simulated by using COMSOL Multiphysics and finite-difference time-domain (FDTD) simulation, respectively. We compare the heat distribution of the planar and tubular VO_2 nanomembrane under thermal radiation on a thick substrate. The elevated heat of the planar nanomembrane was rapidly transferred directly down from the VO_2 nanomembrane to the substrate. Therefore, the temperature of the planar VO_2 nanomembrane is basically the same as that of the substrate (fig. S1A). However, the temperature of the VO_2 tube on the substrate is higher than that of the substrate, as shown in Fig. 1D. This is because the heat transfers between the VO_2 tube and the substrate is greatly limited. The tubular geometry structure can greatly reduce heat transfer from the thermally sensitive VO_2 nanomembrane to substrate, which is one of the key factors in designing high-performance bolometers (*22*). Since bolometers often operate in the long-wave infrared spectrum, limited absorption of heat in atomically thin nanomembranes has always been a great challenge (*23*). Fortunately, the tubular structure can provide an optical microcavity with multiple reflections. During each reflection, a portion of the infrared light is absorbed by the tube wall, and thereby the total absorption in the tubular cavity is remarkably enhanced (*24*). In Fig. 1E, the optical coupling profile under 8-μm incident light is demonstrated, and an electromagnetic field enhancement is formed inside the chamber of the VO_2 tube (fig. S2). In planar nanomembrane device, however, light passing through the thermosensitive VO_2 nanomembrane will travel along the substrate and will not be reabsorbed (fig. S1B). Therefore, tubular bolometers are more advantageous for ultrabroad infrared spectrum detection.

One-step rolling fabrication of VO_2 microtubes

In this work, the VO_2 nanomembrane with a thickness of ~60 nm was sputtered on a 4-inch silicon wafer with 500-nm thermal SiO_2 by using magnetron sputtering at a substrate temperature of 500°C, as shown in Fig. 2A. The flatness of the as-grown VO_2 nanomembrane was confirmed by atomic force microscopy, and the corresponding root mean square roughness is 2.8 nm over a range of 30×30 μm^2 (fig. S3). Meanwhile, as a multivalent metal, the valence state of V in the as-grown nanomembranes is proved by Raman spectroscopy (*25*) and x-ray reflection diffraction (fig. S4) (*26*, *27*). The characteristics of VO_2 metal-insulator phase transition are characterized by temperature-variable Raman spectroscopy (fig. S5) and temperature-variable resistance, as shown in Fig. 2B, and the TCR of the VO_2 nanomembrane at room temperature (RT) is 1.7% K^{-1} (fig. S6). Furthermore, during the cooling process from growth temperature to RT, strain was introduced into the VO_2 nanomembrane due to the mismatch between thermal expansion coefficients of VO_2 and SiO_2. As the excitation wavelength increases, the characteristic peaks of VO_2 exhibit red shifts (Fig. 2C), indicating that compressive strain is introduced into the VO_2 nanomembrane (*28*, *29*), and the compressive strain on the VO_2 nanomembrane estimated by Raman spectroscopy is 0.88% (note S1). In the present work, we used the rolled-up technique to fabricate tubular bolometers, and the fabrication process is shown in Fig. 2D: (i) The VO_2 nanomembrane is grown on the substrate by magnetron sputtering. (ii) The 40-nm Cr layer is grown on VO_2 by e-beam evaporation as additional strain layer and electrode for the bolometer. Then, part of VO_2 is removed by reactive ion etching (RIE) as an etching window. Through photolithography, only the VO_2 nanomembranes and the etching window are exposed, while the metal pads are protected from hydrofluoric acid solution corrosion by photoresists. (iii) Subsequently, the SiO_2 layer was selectively etched by 10% hydrogen fluoride solution. The VO_2/Cr layer is released from the substrate and rolls up into a tubular structure driven by the strain gradient, as shown in Fig. 2E. Compared with previous microbridge (*18*, *19*) and pellicle-supported (*7*, *30*) structures, the fabrication process of tubular structure is simpler and costless (figs. S7 and S8). Figure S9 shows the quantitative relationship of the curvature control for the VO_2/Cr hybrid material system. Comparison of characteristics and applications of self-rolled tubes is shown in table S1. The side view of VO_2 tube (Fig. 2F) indicates that the nanomembrane rolls up to form a rounded circle without slumping. To check the cross section of the sample, a curved VO_2/Cr bilayer was cut at the top of the tube by focused ion beam etching, along the direction marked by the red line in Fig. 2F, and the sample was removed from the tube (figs. S10 and S11). The cross section of the triple-wall microtubes observed by TEM is shown in Fig. 2G. In this device, thin overlapping layers are observed in high-resolution images of the VO_2/Cr interface and corresponding characteristic element maps are obtained by energy-dispersive x-ray spectroscopy (EDS) (Fig. 2H). A fast growth rate (~0.1 nm/s) is required for growing Cr layer that can provide tensile strain (*31*). The formation of amorphous alloys at the VO_2/Cr interface leads to a large increase in the density of defect states, which may lead to increased device noise, trapped photogenerated carriers, and delayed response time. Furthermore, there is a gap of tens of nanometers between the VO_2/Cr layers, which does not impair the thermal insulation (fig. S12) and light trapping effects (fig. S13) of the bolometers. Moreover, the VO_2 microtubes undergo slight deformation, resulting in the formation of oval-shaped microtubes, without compromising the effectiveness of light trapping (fig. S14).

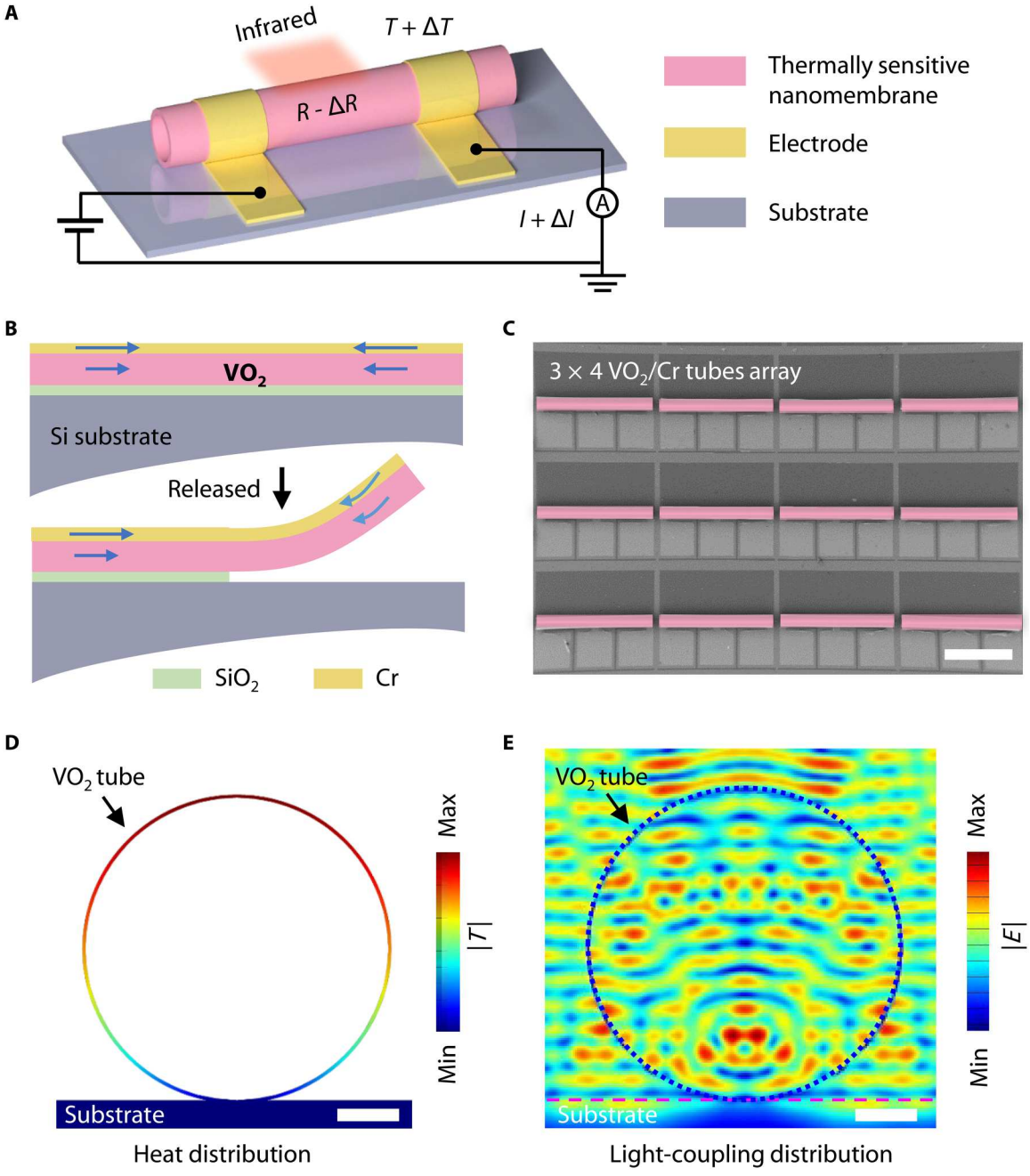

Fig. 1. 3D architecture and working principle of tubular bolometers. (**A**) Perspective-view schematic of the tubular bolometer and its responses to incident infrared light. (**B**) Illustration of VO_2/Cr bilayers with compressive strain on silicon wafers before and after removal of SiO_2 sacrificial layer. (**C**) SEM image of a 3 × 4 array of VO_2/Cr microtubes. Scale bar, 500 μm. (**D**) Simulation of heat distribution of the microtube under the radiation of a heat source (power, 1 mW). Scale bar, 10 μm. (**E**) Simulation of electromagnetic field distribution of the microtube under the illumination of a vertical incident infrared light (wavelength, 8 μm). Scale bar, 10 μm.

To explore the metal-insulator phase transition of rolled-up VO_2 nanomembranes, we performed in situ temperature-changing high-resolution atomic phase characteristics on the curved VO_2 nanomembranes. Figure 2I shows the atomic structure of monoclinic VO_2 observed by high-angle annular dark-field–scanning TEM (STEM) at RT. The inset is the corresponding selected-area electron diffraction (SEAD) pattern at the crystallographic axes of [2, $\bar{1}$, 1], and the (011) and (11$\bar{1}$) planes are marked in bright colors. The interplanar spacing of (011) is 0.327 nm, and that of (11$\bar{1}$) is 0.353 nm. When the temperature is increased from RT to 40°C, the atomic structure of VO_2 transits from monoclinic phase to rutile phase, as shown in Fig. 2J. The inset is the corresponding SEAD pattern with the crystallographic axis directions of [1, 1, $\bar{3}$]. The interplanar spacings of (1$\bar{1}$0) and (211) planes (marked in bright colors) are 0.329 and 0.175 nm, respectively. These parameters are highly consistent with standard VO_2 crystals. The atomic

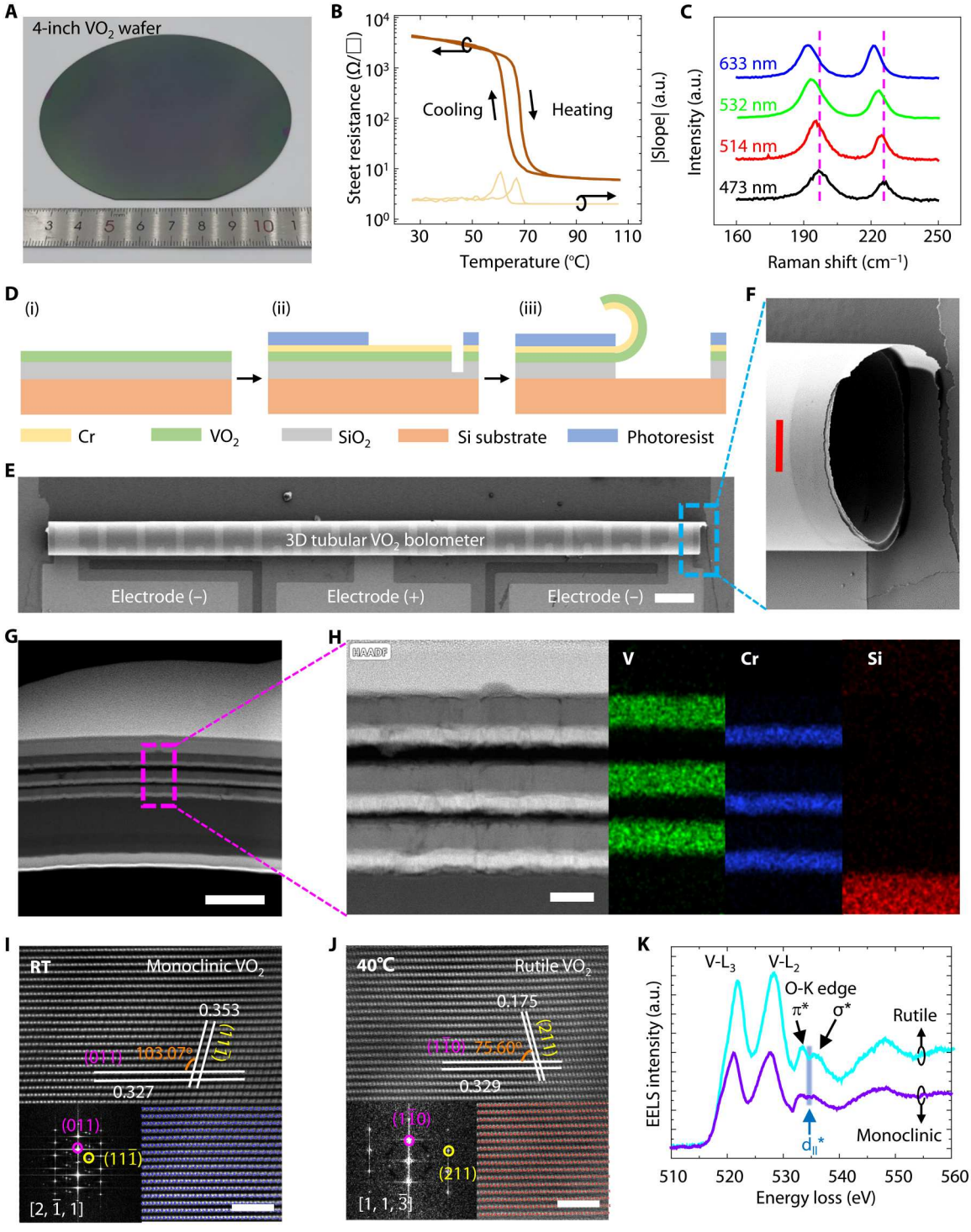

Fig. 2. Fabrication and characterization of rolled-up VO_2 nanomembrane. (**A**) Optical image of VO_2 nanomembranes grown on a 4-inch silicon substrate. (**B**) Sheet resistance of the VO_2 nanomembranes as a function of temperature. The lower lines show the abs(slope) of the resistivity. (**C**) Raman spectra of the VO_2 nanomembrane excited by lasers with wavelengths of 633, 532, 514, and 473 nm. a.u., arbitrary units. (**D**) Schematic illustrating the preparation process of VO_2 microtube. (**E**) Focused view of a single microtube. Scale bar, 50 μm. (**F**) Side view of the microtube. (**G**) TEM image of the multilayer VO_2/Cr microtube wall. Scale bar, 500 nm. (**H**) High-resolution cross-sectional STEM image of the VO_2/Cr microtube and corresponding elemental distribution. Scale bar, 100 nm. STEM images with corresponding fast Fourier transform patterns and standard atomic structures (O atoms are not shown) of the rolled-up VO_2 nanomembrane at RT (**I**) and 40°C (**J**). Scale bars, 2 nm. (**K**) EELS spectra of monoclinic and rutile VO_2 nanomembranes.

phase crystal structure and lattice parameters change slightly when the in situ temperature is continuously increased to 50°, 60°, 70°, and 80°C (fig. S15). Before and after the VO_2 phase transition, the change of atomic arrangement and SEAD pattern can be seen intuitively (*32*, *33*), which can also be observed in TEM (fig. S16). At RT, the V atoms in the monoclinic VO_2 appear dimerized along the *c* axis with a slight twist, which produces fully occupied bonds $d_{\parallel}$ and fully empty anti-bonds $d_{\parallel}^{*}$. The Fermi level passes between $d_{\parallel}^{*}$ and $d_{\parallel}$, resulting in a bandgap of about 0.7 eV (*34*, *35*), so VO_2 exhibits semiconducting properties at low temperature. When the temperature is higher than phase transition temperature, VO_2 of the rutile phase is metallic. $d_{\parallel}$ overlaps with the π bond, and $d_{\parallel}$ is penetrated by the Fermi level (fig. S17). The electron energy loss spectrum (EELS) of monoclinic and rutile VO_2 nanomembranes is presented in Fig. 2K. The π^{*} peak and O^{*} peak at the O—K edge of monoclinic VO_2 nanomembranes are relatively flat (*32*, *36*, *37*). In addition, the depression after heating represents the appearance of $d_{\parallel}^{*}$ in rutile VO_2 nanomembrane. That is, VO_2 is transformed from semiconductor phase to metallic phase when temperature rises to 40°C (fig. S17).

Geometry-dependent thermal insulation of VO_2 nanomembranes

To achieve high response metrics in bolometers, we need a comprehensive understanding of the geometrical dependence of metal insulation phase transition and electrical characteristics of the VO_2 nanomembrane. Previous studies have shown that the metal-insulator phase transition of VO_2 can be regulated by strain, electric field, etc. For instance, compressive (tensile) strain can reduce (increase) the phase transition temperature of VO_2 (*31*, *38*–*40*). In addition, the reversible metal-insulator phase transition of VO_2 can be directly induced by applying a voltage to generate Joule heat. The dissipation of the Joule heat generated in the VO_2 nanomembrane mainly includes heat conduction to the thick substrate and heat radiation to the atmosphere. Figure 3A shows schematic of an unreleased VO_2 nanomembrane device, and its electrical properties are measured at different substrate temperatures from 25° to 80°C with a 5°C step (Fig. 3D and fig. S18). Current changes were found only when the temperature reached around the normal VO_2 phase transition temperature (~68°C). We extracted the current under 0.1 V at different temperatures (Fig. 3G), which indicates that the Joule heat generated in the unreleased VO_2 nanomembranes is dissipated very quickly, and not sufficient to change the phase transition temperature of VO_2. After the VO_2 nanomembrane is released, as shown in Fig. 3B, both sides of VO_2 are exposed to the air, and only a small part of the VO_2 nanomembrane is attached to the substrate. As shown in Fig. 3E, applying a voltage less than 5 V can cause the metal-insulator phase transition at RT. We define the voltage at which VO_2 undergoes a metal-insulator phase transition as V_{MIT}. V_{MIT} (corresponding to phase transitions from insulation to metal and metal to insulation) at different temperatures (fig. S19) is shown in Fig. 3H, and V_{MIT} obviously decreases with increasing substrate temperature. When the substrate temperature exceeds 50°C, it is difficult to find a distinguishable V_{MIT}. This may be caused by the decrease in the phase transition temperature due to the strain in the released VO_2 nanomembranes. These experimental results indicate that the thermal conduction between the released VO_2 and the substrate is greatly reduced, and a metal-insulator phase transition can occur at lower temperature with voltage driving. It should be noted that at 50°C, V_{MIT} increases. This phenomenon can be attributed to two state transitions of VO_2 nanofilms under bias voltage/temperature regulation, i.e., planar and bending, which lead to loss of Joule heat. Figure 3C shows that the released VO_2 nanomembrane rolls up into microtube. Compared to the released VO_2 nanomembrane that does not roll into tube, the area of nanomembrane directly exposed to the air in the tube is greatly reduced because of the formation of multilayered walls during self-rolling, as shown in Fig. 2B. In addition, voltage-driven metal to insulation phase transitions of VO_2 can also be realized in tubular devices (Fig. 3F and fig. S20). The V_{MIT} required to drive the metal-insulator phase transition of the tubular VO_2 nanomembranes is smaller, which is linearly dependent to temperature (Fig. 3I). No deformation of VO_2 microtubes was observed when the phase transition occurred, indicating that the VO_2 nanomembranes with the tubular structure have excellent thermal insulation, thermal retention properties, and higher mechanical stability. Furthermore, VO_2 microtubes with more winding numbers require a smaller V_{MIT} (fig. S21). This is because, under the same heat loss conditions, the tube with more rotations can generate more Joule heat to drive the phase transition of VO_2.

Optoelectronic characteristics of tubular VO_2 bolometers

We investigated the absorbance of the VO_2 microtubes, and the result displays strong temperature dependence. In the experiment, the VO_2 nanomembrane was transferred to GaF_2 substrate for in situ variable temperature Fourier transform infrared (FTIR) test (fig. S22). At RT, the single-layered VO_2 nanomembrane has a low absorbance over the entire spectral range; however, it shows an increase in absorbance with increasing temperature (*41*). Furthermore, a sharp increase (decrease) in the absorbance of VO_2 can be observed during heating (cooling), which is consistent with the behavior of resistance changing during VO_2 phase transition (fig. S23). The temperature-dependent absorption characteristics of the double-layered VO_2 nanomembrane are coherent with the single-layered VO_2 nanomembrane (fig. S24), but the absorbance is about twice of the single-layer VO_2 nanomembrane (fig. S25). The low absorbance of the planar VO_2 nanomembrane results in the unquestionably low detection performance of infrared photodetectors (figs. S26 and S27). Similarly, there is also a temperature-dependent absorbance in the tubular VO_2 nanomembrane, and the temperature at which the absorbance decreases drastically is consistent with the phase transition temperature of the tubular VO_2 nanomembrane (fig. S28). The absorbance of the tubular VO_2 nanomembrane was greatly improved across the entire spectrum. The phase transition temperature of the VO_2 nanomembranes decreases when subjected to compressive strain. To clearly demonstrate that the increased absorbance of the tubular VO_2 nanomembrane is mainly due to its tubular geometry, we present the absorbance of planar single-layer VO_2 nanomembrane, curved single-layer VO_2 nanomembrane, and single-walled VO_2 tube at RT in Fig. 4A. The absorbance calculated by Lambert Beer's law exceeds 1, which means that the actual absorbance exceeds 90% (*42*). Compared with the planar VO_2 nanomembrane, the absorbance of the curved VO_2 nanomembrane is almost doubled, while the absorbance of the tubular VO_2 nanomembrane in the long-wave infrared is more than 20 times higher, as shown in Fig. 4B.

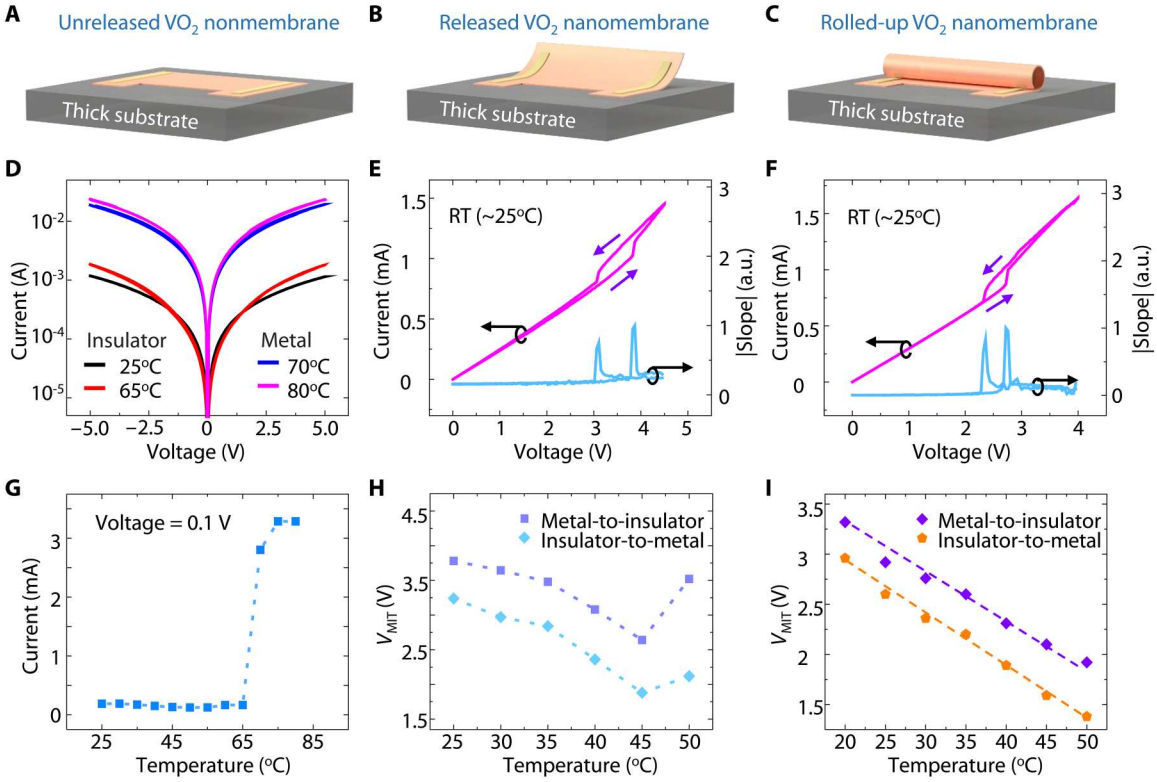

Fig. 3. Metal-insulator phase transition of the VO_2 nanomembranes driven by temperature and voltage. Schematic diagram of unreleased (**A**), released (**B**), and rolled-up (**C**) VO_2 nanomembranes on chips. (**D**) Current-voltage characteristic curves of the unreleased VO_2 nanomembrane device under different heating temperatures. VO_2 nanomembranes are semiconductor at 25° and 60°C and metal at 70° and 80°C. Current-voltage characteristic curves of the released (**E**) and rolled-up (**F**) VO_2 nanomembranes measured at RT. The lower curves show the absolute value of the current-voltage slope. (**G**) Current of unreleased VO_2 nanomembranes at 0.1 V at different temperatures. A sudden change in current between 65° and 70°C indicates metal-insulator phase transition in the VO_2 nanomembrane. V_{MIT} of freestanding (**H**) and rolled-up (**I**) VO_2 nanomembranes as a function of heating temperature.

Figure 4C shows the electrical properties of a VO_2 microtube. During full cycles of voltages from 0 to 3 V and 3 to 0 V, VO_2 transitions from monoclinic to rutile and then back to monoclinic. The phase change voltage is between 1 and 1.5 V. To analyze the noise sources of the device, we measured the current noise in the dark current, as shown in Fig. 4D. The results show that generation-recombination (G-R) noise and $1/f$ noise are the main noise sources for this device at low and high frequencies, respectively (*43*, *44*). In addition, the current noise of the device increases with increasing applied bias voltage (fig. S29), which is probably due to the Joule heat generated at high voltages. To characterize the response time of the bolometer, frequency-dependent measurements of the photocurrent increment were performed and the results are shown in Fig. 4E. Low-frequency devices are affected by G-R noise resulting in a trend of $I_p \sim 1/f^2$, when the photocurrent of the device at high frequency is dominated by $1/f$ noise. The photoresponse current $R_I(\omega)$ can be explained and approximated (*45*) by $R_I(\omega) = F(\omega)/\sqrt{(1 + \tau^2\omega^2)}$, where $F(\omega)$ is a rational polynomial term, mainly related to the thermal propagation characteristics of VO_2, and ω is the modulation frequency. We get a response time constant τ = 14.9 ms, and the tubular VO_2 bolometer exhibits a noise equivalent power of 1.79 $nW/\sqrt{Hz}$ and a calculated NETD of 64.6 mK (note S2). Figure 4F shows the temporal response of the photocurrent under laser illumination of different wavelengths. The corresponding rise and decay times are 3.1 and 1.7 ms at 520 nm, 1.8 and 1.4 ms at 1650 nm, and 2.3 and 2.1 ms at 4600 nm (fig. S30). Figure 4G shows that the detectivity (D^*) of the bolometer is calculated with the formula (*46*, *47*) $D^* = \frac{R}{\sqrt{\left(\frac{4k_bT}{R'A} + \frac{2eI_{dark}}{A}\right)}}$, where e is the unit charge, R' is the bias resistance, A is the effective area of the device, I_{dark} is the dark current, and R is the photoresponsivity, and no wavelength-selective properties are observed. The calculated average detectivity is ~2×10^8 cm $Hz^{0.5}$ W^{-1}, which is slightly overestimated for lacking consideration of $1/f$ noise. Figure 4H shows the peak detectivity of commercially available high-performance HgCdTe detectors, the emerging InAs/InAsSb superlattice, and several typical thermal detectors. Compared with long-wave infrared detectors operating at RT, our tubular bolometers have performance advantages, but are slightly inferior to photon detectors and superconducting bolometers operating at low temperatures. In the long-wavelength infrared range, the theoretical performance limit of thermal detectors is closest to that of photon detectors. With further optimization, the microtube bolometer could be a very promising structural paradigm to help thermal detectors bridge the performance gap to photon detectors.

The performance merits of a tubular VO_2 bolometer are further demonstrated and compared to typical commercially available long-wavelength infrared photodetectors. The tubular geometry is anisotropic to the electric vector of electromagnetic waves, like nanowires

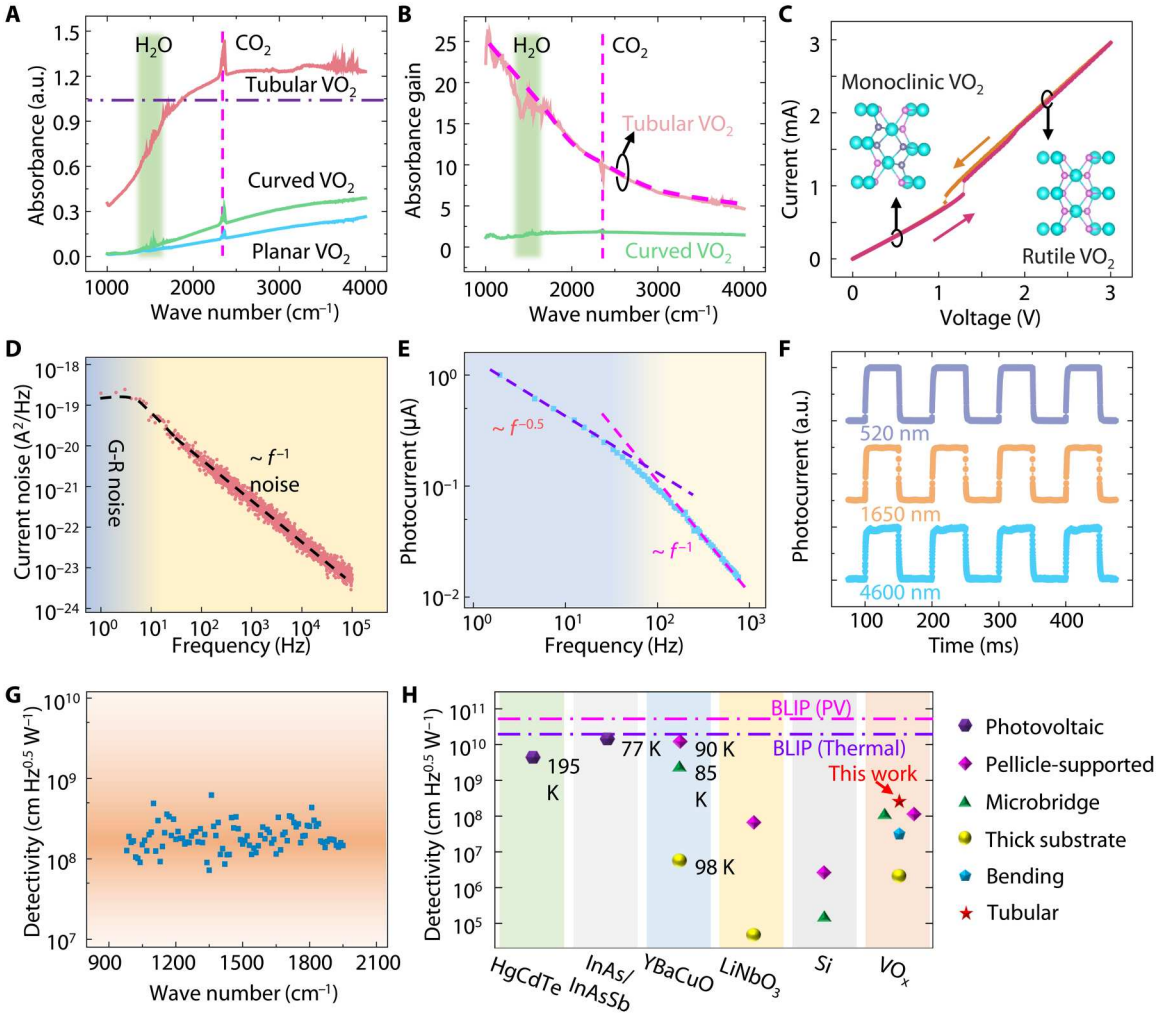

Fig. 4. Photoresponse performance of tubular VO_2 bolometers. (**A**) Absorbance of planar VO_2 nanomembrane, curved VO_2 nanomembrane, and single-walled VO_2 microtubules at RT, including fluctuations in the absorption of CO_2 and H_2O in air. The absorption of CO_2 and H_2O in the atmosphere caused fluctuations of 2375 to 2350 cm^{-1} and 1750 to 1200 cm^{-1}, respectively. (**B**) Increase in absorbance of curved VO_2 and tubular VO_2 relative to planar VO_2. (**C**) Current-voltage characteristics of a multi-turn VO_2 microtube and voltage-driven metal-insulator phase transition. Inset is a ball-and-stick model of monoclinic (rutile) VO_2 at low voltage (high voltage). (**D**) Current noise of a tubular VO_2 bolometer varied with frequency (f). The device is measured at RT, and the voltage is set as 0.5 V. (**E**) Photocurrent response dependence of the bolometer as a function of frequency (f). (**F**) Response time of the device under 520-, 1650-, and 4600-nm laser illumination with $V = 0.5$ V. (**G**) Detectivity of the tubular VO_2 bolometer as a function of the wave number, and the voltage is set as 0.5 V. The detectivity is up to ~2×10^8 cm $Hz^{0.5}$ W^{-1} in ultrabroad infrared spectrum. (**H**) Detectivity comparison of the tubular VO_2 bolometer with other long-wavelength infrared photodetectors. The background-limited infrared performance (BLIP) of photovoltaic and thermal infrared photodetectors at 8 μm is shown by dashed-dotted lines. HgCdTe, InAs/InAsSb, and YBaCuO work at low temperatures, as indicated in the figure.

(*48*), which has the potential for polarized light detection without assistance of optical lenses. The test setup illustrated in Fig. 5A was used to study the polarization-dependent response. Figure 5B shows the relationship between the photocurrent and polarization angle of the tubular bolometer. The angle of incoming polarized light causes a periodic variation in the photocurrent. The dichroic ratio of the tubular devices can be obtained by using a fitting function to determine the device's capacity for polarization detection. Under 4600-nm light, the tubular bolometer exhibits a dichroic ratio of 1.17. In addition, the tubular geometry also provides an opportunity for wide-angle detection from the direction that is perpendicular to the tube axis (*24*). Figure 5C is a schematic diagram of an axial section of the tube with a 520-nm laser irradiated on the tube at an angle of θ_1. By rotating the laser (fig. S31), the tubular bolometer presents an angle-independent photocurrent within −75° to 75°, as shown in Fig. 5D. The simulation results show that the VO_2 microtubes can also trap light with incident angles of 90°, 60°, 45°, and 30° (fig. S32). Figure S33A is a schematic vertical axial cross-sectional view of the tube where the laser is irradiated on the tube at an angle θ_2. By measuring photocurrent via rotating the laser around the tube, the tubular bolometer exhibits a pronounced angle-dependent photocurrent omnidirectionally, as shown in Fig. 5D, which is consistent with the angle-dependent properties of planar devices, and the photocurrent can be explained by the formula $I_p = I_{p,\theta=90°} \times \cos \theta_2$ (fig. S33B). However, the tubular geometry still retains the trapping effect for light (fig. S34).

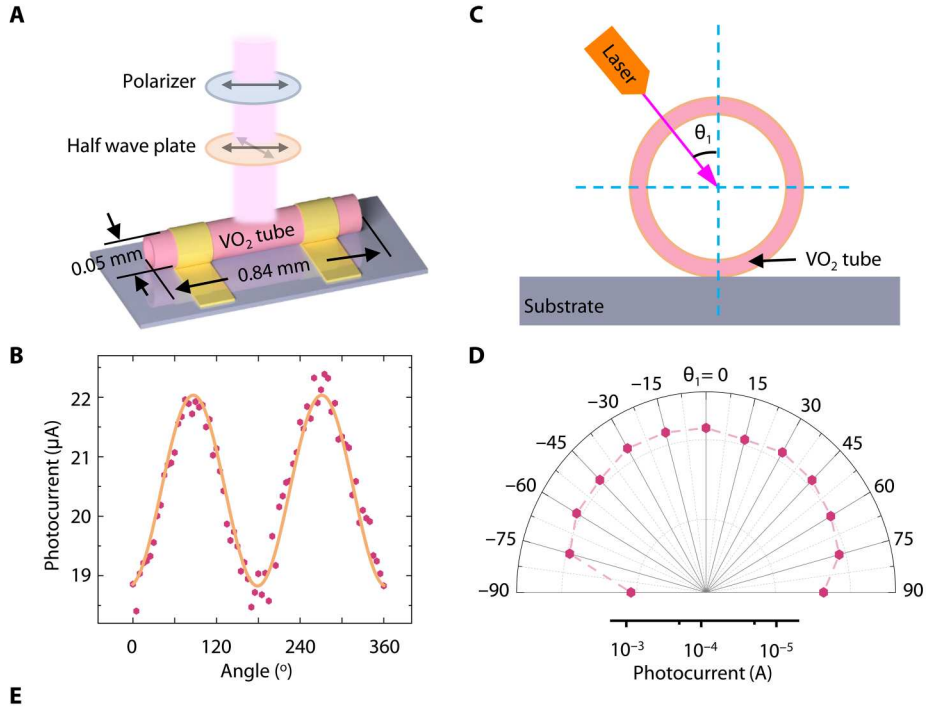

E

Sensor	HgCdTe detector	Pyroelectric detector	Tubular bolometer
Acceptance angle	35°	45°	150°
Effective sensor area	1 × 1 mm^2	1.4 × 1.0 mm^2	0.84 × 0.05 mm^2
Reference	THORLABS	INFRATEC	This work

Fig. 5. Polarization and omnidirectional detection characteristics of 3D tubular bolometers. (**A**) Schematic of a tubular VO_2 bolometer irradiated by polarized light. (**B**) Photocurrent as a function of the polarization angle of incident light. The wavelength is 4600 nm. The solid line represents fitting using a sinusoidal function $I_{ph}(\delta) = I_{py}\cos^2(\delta + \phi) + I_{px}\sin^2(\delta + \phi)$. The fitted dichroic ratio is 1.17. (**C**) Schematic cross section of a tubular VO_2 bolometer irradiated by light at an angle θ_1 along the direction perpendicular to the tube axis. (**D**) Angle-independent photocurrent at different light incident angles. (**E**) Comparison of the acceptance angle and effective sensor area of our tubular VO_2 bolometer to commercially available HgCdTe (photovoltaic) and pyroelectric (thermal) detectors.

Long-wavelength infrared is often used for safety prevention and control in civilian fields, such as emergency search and rescue and forest fire prevention. The detection distance of long-wave detectors can reach kilometers or more, but the viewing angle is often limited by the optical lens and its own area. Therefore, it is of far-reaching significance to realize wide-angle detection to broaden the observation range of infrared detectors. Figure 5E shows a comparison of acceptance angle and effective sensor area to other advanced commercially available infrared detectors. Our tubular bolometer enables large detection angle in a small footprint. A bolometer with a tubular geometry holds great promise for wide-angle and broad-spectrum polarization photodetection at RT.

DISCUSSION

We have designed and fabricated a proof-of-concept device architecture—tubular VO_2 bolometers by a one-step rolling approach. The introduction of tubular geometry into nanomembrane bolometers improves thermal insulation, enhances light absorption, and enables polarization-sensitivity and omnidirectional light detection. In addition, the compressive strain reduces the metal-insulator phase transition temperature of VO_2, making the rolled-up VO_2 nanomembrane more sensitive to thermal signals. For an emerging structural paradigm of bolometers, the detectivity of 2×10^8 cm $Hz^{0.5}$ W^{-1}, response times of ~2.0 ms, and calculated NETD of 64.5 mK are excellent starting points for further improving the performance of tubular device by optimizing material quality, 3D packaging, etc. Our tubular bolometer is a pioneering integrated sensing device, and it opens the possibility to explore numerous applications in the long-infrared region with tubular device structure and design, which will potentially change the current civil infrared market landscape.

MATERIALS AND METHODS

Growth of VO_2 nanomembranes and fabrication of tubular VO_2 bolometers

The 4-inch silicon substrate covered with 500-nm SiO_2 was cleaned with acetone and deionized water. VO_2 nanomembranes are sputtered on silicon substrate by magnetron sputtering at 500°C for 700 s in argon-oxygen flux. The argon-oxygen ratio is 36:60, and the sputtering power is 200 W. The electrodes were defined by photolithography (HEIDELBERG, UPG501), and Cr was deposited by electron beam evaporator. The etching window is etched by RIE for 100 s [30 standard cubic centimeters per minute (sccm) Ar and 30 sccm CF_4 flow, 300 mtorr chamber pressure, and 100 W etching power]. The VO_2 nanomembranes were released and rolled up in 10% hydrofluoric acid solution for 3 min. Last, the rolled-up microtubes are dried in a critical point drying (Leica CPD030 Critical Point Dryer).

Material characterizations

A LabRam HR800 from HORIBA spectrometer and heating stage (Linkam LTSE420) were used for Raman measurements. VO_2 nanomembranes were also characterized by XRD (Bruker D8 DISCOVER). The absorbances of VO_2 nanomembranes were measured by FTIR spectroscopy (Thermo Fisher Scientific, Nicolet IS5, BRUKER TENSOR II). The morphologies of VO_2 tubes were first characterized by scanning electron microscopy (SEM; JEOL JSM-6701F), and the TEM and EDS measurements were performed by JEOL JEM2100F TEM with EX-24063JGT EDS.

Electrical and optoelectronic characterizations

The electrical measurements were performed by using a commercial KEYSIGHT B2902B at RT and under ambient conditions. The measurement of photocurrent was carried out with a modulated laser beam, and the photocurrent signal was acquired by a lock-in amplifier (Stanford SR830) and a current amplifier (Stanford SR570). Polarized photocurrent measurement was taken by an MStarter 200 optoelectronic measurement system from Maita Optoelectronic Technology Co. Ltd. In the polarization test, the linearly polarized light is focused onto the upper surface of the self-rolled VO_2 microtubes through the lens, and the substrate is not exposed to light. During the test of omnidirectional detection, a large laser light spot completely covers the VO_2 microtubes and part of the substrate. The noise was measured by a noise measurement system (PDA NC300L, 100-kHz bandwidth).

Thermal and optical simulation

The thermal simulation was realized by COMSOL Multiphysics, in which we considered the heat flow from incident laser as a Gaussian function distribution heat source that is vertical to the substrate. Because the spot radius of laser (~mm) is far larger than the size of microtube (~μm), the laser can be considered as uniformly distributed on microtube with power of 1 mW to obtain the transient thermal response of the device. As for solid, the energy conservation equation can be written as

$$\rho C_p\left(\frac{\partial T}{\partial t}+u\cdot\nabla T\right)=\nabla\cdot(k\nabla T)+W_\sigma+Q \quad (1)$$

where ρ is the density, C_p is the heat capacity at constant pressure, T is the temperature, k is the thermal conductivity, t is the time, u is the displacement, W_σ is the heat source generated by solid compression or expansion during temperature change, and Q is the heat absorbed by the system. During the heating process, the temperature changes of tube and substrate are relatively small, and the coefficient of thermal expansion α is about 10^{-5}, so W_σ in the process is negligible. The equation is then simplified to

$$\rho C_p\left(\frac{\partial T}{\partial t}+u\cdot\nabla T\right)=\nabla\cdot(k\nabla T)+Q \quad (2)$$

Optical simulation of VO_2 nanomembranes was performed on the basis of the finite element method by using FDTD approach to exhibit the light trapping in VO_2 tube. The incident light is considered as plane wave, with wavelengths from 1 to 10 μm and a step of 1 μm. The boundary condition of substrate side and its opposite side was set as perfectly matched layer, while boundary condition of other two sides that is vertical to substrate was set as periodic because the tubes are identical in the tube arrays. The wave equation of plane wave can be written as

$$\nabla\times(\nabla\times E)-k_0^2\varepsilon_r E=0 \quad (3)$$

where E is the electric field, k_0 is the imaginary part of refractive index, and ε_r is the relative dielectric constant. The relative dielectric constant is calculated by

$$\varepsilon_r=(n-ik)^2 \quad (4)$$

where n is the refractive index and k is the extinction coefficient.

Supplementary Materials

This PDF file includes:

Figs. S1 to S34
Table S1
Notes S1 and S2
References

REFERENCES AND NOTES

1. A. Bendada, K. Cole, M. Lamontagne, Y. Simard, A hollow waveguide infrared thermometer for polymer temperature measurement during injection moulding. *J. Opt. A Pure Appl. Opt.* **5**, 464–470 (2003).
2. A. Seward, S. Ashraf, R. Reeves, C. Bromley, Improved environmental monitoring of surface geothermal features through comparisons of thermal infrared, satellite remote sensing and terrestrial calorimetry. *Geothermics* **73**, 60–73 (2018).
3. N. Aggarwal, M. Garg, V. Dwarakanathan, N. Gautam, S. S. Kumar, R. S. Jadon, M. Gupta, A. Ray, Diagnostic accuracy of non-contact infrared thermometers and thermal scanners: A systematic review and meta-analysis. *J. Travel Med.* **27**, taaa193 (2020).
4. M. Siciliani de Cumis, S. Viciani, S. Borri, P. Patimisco, A. Sampaolo, G. Scamarcio, P. De Natale, F. D'Amato, V. Spagnolo, Widely-tunable mid-infrared fiber-coupled quartz-enhanced photoacoustic sensor for environmental monitoring. *Opt. Express* **22**, 28222–28231 (2014).
5. M. T. Eismann, A. D. Stocker, N. M. Nasrabadi, Automated hyperspectral cueing for civilian search and rescue. *Proc. IEEE* **97**, 1031–1055 (2009).
6. R. Chatterjee, F. Matsuno, Robot description ontology and disaster scene description ontology: Analysis of necessity and scope in rescue infrastructure context. *Adv. Robot.* **19**, 839–859 (2012).
7. V. Y. Zerov, V. G. Malyarov, I. A. Khrebtov, Y. V. Kulikov, I. I. Shaganov, Uncooled membrane-type linear microbolometer array based on a VO_x film. *J. Opt. Technol.* **68**, 428–431 (2001).
8. P. G. Datskos, S. Rajic, I. Datskou, Photoinduced and thermal stress in silicon microcantilevers. *Appl. Phys. Lett.* **73**, 2319–2321 (1998).
9. F. Dong, Q. Zhang, D. Chen, Z. Miao, Z. Xiong, Z. Guo, C. Li, B. Jiao, X. Wu, Uncooled infrared imaging device based on optimized optomechanical micro-cantilever array. *Ultramicroscopy* **108**, 579–588 (2008).

10. M. Steffanson, K. Gorovoy, V. Ramkiattisak, T. Ivanov, J. Król, H. Hartmann, I. W. Rangelow, ARCH-type micro-cantilever FPA for uncooled IR detection. *Microelectron. Eng.* **98**, 614–618 (2012).
11. A. Bigioli, G. Armaroli, A. Vasanelli, D. Gacemi, Y. Todorov, D. Palaferri, L. Li, A. G. Davies, E. H. Linfield, C. Sirtori, Long-wavelength infrared photovoltaic heterodyne receivers using patch-antenna quantum cascade detectors. *Appl. Phys. Lett.* **116**, 161101 (2020).
12. R. E. Flannery, J. E. Miller, Status of uncooled infrared imagers. *Proc. SPIE*, 379–395 (1992).
13. A. S. Oleinik, D. M. Maslov, Bolometer with thermosensitive layer made of vanadium oxide VO_x. *Nanotechnol. Russ.* **7**, 227–237 (2012).
14. A. Subrahmanyam, Y. B. K. Reddy, C. L. Nagendra, Nano-vanadium oxide thin films in mixed phase for microbolometer applications. *J. Phys. D Appl. Phys.* **41**, 195108 (2008).
15. V. Y. Zerov, V. G. Malyarov, Heat-sensitive materials for uncooled microbolometer arrays. *J. Opt. Technol.* **68**, 939–948 (2001).
16. A. Rogalski, Infrared detectors: An overview. *Infrared Phys. Technol.* **43**, 187–210 (2002).
17. F. Niklaus, A. Decharat, C. Jansson, G. Stemme, Performance model for uncooled infrared bolometer arrays and performance predictions of bolometers operating at atmospheric pressure. *Infrared Phys. Technol.* **51**, 168–177 (2008).
18. C. H. Chen, Z. P. Zhou, Optical phonons assisted infrared absorption in VO_2 based bolometer. *Appl. Phys. Lett.* **91**, 011107 (2007).
19. G. Li, N. Y. Yuan, J. H. Li, X. S. Chen, Thermal simulation of micromachined bridge and self-heating for uncooled VO_2 infrared microbolometer. *Sens. Actuators A Phys.* **126**, 430–435 (2006).
20. P. Deepak Raj, S. Gupta, M. Sridharan, Nanostructured V_2O_5 thin films deposited at low sputtering power. *Mater. Sci. Semicond. Process.* **39**, 426–432 (2015).
21. P. De Moor, Y. Creten, C. Goessens, B. Grietens, V. Leonov, J. Vermeiren, C. Van Hoof, Thermal infrared detection using linear arrays of poly SIGe uncooled microbolometers, *Proceedings of the 12th IEEE International Conference on Fuzzy Systems* (IEEE, 2003).
22. A. Rogalski, *Infrared Detectors* (CRC Press, 2000).
23. Y. Chen, C. Tan, Z. Wang, J. Miao, X. Ge, T. Zhao, K. Liao, H. Ge, Y. Wang, F. Wang, Y. Zhou, P. Wang, X. Zhou, C. Shan, H. Peng, W. Hu, Momentum-matching and band-alignment van der Waals heterostructures for high-efficiency infrared photodetection. *Sci. Adv.* **8**, eabq1781 (2022).
24. H. Wang, H. L. Zhen, S. L. Li, Y. L. Jing, G. S. Huang, Y. F. Mei, W. Lu, Self-rolling and light-trapping in flexible quantum well-embedded nanomembranes for wide-angle infrared photodetectors. *Sci. Adv.* **2**, e1600027 (2016).
25. P. Shvets, O. Dikaya, K. Maksimova, A. Goikhman, A review of Raman spectroscopy of vanadium oxides. *J. Raman. Spectrosc.* **50**, 1226–1244 (2019).
26. R. Shi, J. Wang, X. Cai, L. Zhang, P. Chen, S. Liu, L. Zhang, W. Ouyang, N. Wang, C. Cheng, Axial modulation of metal-insulator phase transition of VO_2 nanowires by graded doping engineering for optically readable thermometers. *J. Phys. Chem. C* **121**, 24877–24885 (2017).
27. R. Balu, P. V. Ashrit, Near-zero IR transmission in the metal-insulator transition of VO_2 thin films. *Appl. Phys. Lett.* **92**, 021904 (2008).
28. X. Li, Y. Wang, B. Xu, X. Zhou, C. Men, Z. Tian, Y. Mei, Rolled-up single-layered vanadium oxide nanomembranes for microactuators with tunable active temperature. *Nanotechnology* **30**, 354003 (2019).
29. J. M. Atkin, S. Berweger, E. K. Chavez, M. B. Raschke, J. Cao, W. Fan, J. Wu, Strain and temperature dependence of the insulating phases of VO_2 near the metal-insulator transition. *Phys. Rev. B* **85**, 020101 (2012).
30. H. Jerominek, F. Picard, N. Swart, M. Renaud, M. Levesque, M. Lehoux, J. Castonguay, M. Pelletier, G. Bilodeau, D. Audet, T. Pope, P. Lambert, Micromachined uncooled VO_2-based IR bolometer arrays. *Proc. SPIE* **2746**, 60–71 (1996).
31. Z. Tian, B. R. Xu, B. Hsu, L. Stan, Z. Yang, Y. F. Mei, Reconfigurable vanadium dioxide nanomembranes and microtubes with controllable phase transition temperatures. *Nano Lett.* **18**, 3017–3023 (2018).
32. F. Sandiumenge, L. Rodriguez, M. Pruneda, C. Magen, J. Santiso, G. Catalan, Metallic diluted dimerization in VO_2 tweeds. *Adv. Mater.* **33**, e2004374 (2021).
33. S. Cheng, M.-H. Lee, R. Tran, Y. Shi, X. Li, H. Navarro, C. Adda, Q. Meng, L.-Q. Chen, R. C. Dynes, S. P. Ong, I. K. Schuller, Y. Zhu, Inherent stochasticity during insulator-metal transition in VO_2. *Proc. Natl. Acad. Sci. U.S.A.* **118**, e2105895118 (2021).
34. K. Liu, S. Lee, S. Yang, O. Delaire, J. Q. Wu, Recent progresses on physics and applications of vanadium dioxide. *Mater. Today* **21**, 875–896 (2018).
35. Z. W. Shao, X. Cao, H. J. Luo, P. Jin, Recent progress in the phase-transition mechanism and modulation of vanadium dioxide materials. *Npg Asia Mater.* **10**, 581–605 (2018).
36. X. W. Lin, Y. Y. Wang, V. P. Dravid, P. M. Michalakos, M. C. Kung, Valence states and hybridization in vanadium oxide systems investigated by transmission electron-energy-loss spectroscopy. *Phys. Rev. B* **47**, 3477–3481 (1993).
37. M. Abbate, F. M. de Groot, J. C. Fuggle, Y. J. Ma, C. T. Chen, F. Sette, A. Fujimori, Y. Ueda, K. Kosuge, Soft-x-ray-absorption studies of the electronic-structure changes through the VO_2 phase transition. *Phys. Rev. B* **43**, 7263–7266 (1991).
38. K. Nagashima, T. Yanagida, H. Tanaka, T. Kawai, Stress relaxation effect on transport properties of strained vanadium dioxide epitaxial thin films. *Phys. Rev. B* **74**, 172106 (2006).
39. M. K. Liu, M. Wagner, E. Abreu, S. Kittiwatanakul, A. McLeod, Z. Fei, M. Goldflam, S. Dai, M. M. Fogler, J. Lu, S. A. Wolf, R. D. Averitt, D. N. Basov, Anisotropic electronic state via spontaneous phase separation in strained vanadium dioxide films. *Phys. Rev. Lett.* **111**, 096602 (2013).
40. J. Cao, E. Ertekin, V. Srinivasan, W. Fan, S. Huang, H. Zheng, J. W. L. Yim, D. R. Khanal, D. F. Ogletree, J. C. Grossman, J. Wu, Strain engineering and one-dimensional organization of metal-insulator domains in single-crystal vanadium dioxide beams. *Nat. Nanotech.* **4**, 732–737 (2009).
41. T. C. Chang, X. Cao, S. H. Bao, S. D. Ji, H. J. Luo, P. Jin, Review on thermochromic vanadium dioxide based smart coatings: From lab to commercial application. *Adv. Manuf.* **6**, 1–19 (2018).
42. X. Sun, Y. Sheng, X. Gao, Y. Liu, F. Ren, Y. Tan, Z. Yang, Y. Jia, F. Chen, Self-powered lithium niobate thin-film photodetectors. *Small* **18**, e2203532 (2022).
43. D. M. Fleetwood, 1/f Noise and defects in microelectronic materials and devices. *IEEE Trans. Nucl. Sci.* **62**, 1462–1486 (2015).
44. U. Sassi, R. Parret, S. Nanot, M. Bruna, S. Borini, D. De Fazio, Z. Zhao, E. Lidorikis, F. H. L. Koppens, A. C. Ferrari, A. Colli, Graphene-based mid-infrared room-temperature pyroelectric bolometers with ultrahigh temperature coefficient of resistance. *Nat. Commun.* **8**, 14311 (2017).
45. X. Wang, H. Shen, Y. Chen, G. Wu, P. Wang, H. Xia, T. Lin, P. Zhou, W. Hu, X. Meng, J. Chu, J. Wang, Multimechanism synergistic photodetectors with ultrabroad spectrum response from 375 nm to 10 μm. *Adv. Sci.* **6**, 1901050 (2019).
46. Y. Chen, Y. Wang, Z. Wang, Y. Gu, Y. Ye, X. Chai, J. Ye, Y. Chen, R. Xie, Y. Zhou, Z. Hu, Q. Li, L. Zhang, F. Wang, P. Wang, J. Miao, J. Wang, X. Chen, W. Lu, P. Zhou, W. Hu, Unipolar barrier photodetectors based on van der Waals heterostructures. *Nat. Electron.* **4**, 357–363 (2021).
47. J. Bullock, M. Amani, J. Cho, Y. Z. Chen, G. H. Ahn, V. Adinolfi, V. R. Shrestha, Y. Gao, K. B. Crozier, Y. L. Chueh, A. Javey, Polarization-resolved black phosphorus/molybdenum disulfide mid-wave infrared photodiodes with high detectivity at room temperature. *Nat. Photon.* **12**, 601–607 (2018).
48. J. Wang, M. S. Gudiksen, X. Duan, Y. Cui, C. M. Lieber, Highly polarized photoluminescence and photodetection from single indium phosphide nanowires. *Science* **293**, 1455–1457 (2001).
49. R. A. Wood, High-performance infrared thermal imaging with monolithic silicon focal planes operating at room temperature, *Proceedings of IEEE International Electron Devices Meeting* (IEEE, 1993).
50. B. F. Andresen, F. Niklaus, G. F. Fulop, C. Jansson, A. Decharat, P. R. Norton, J.-E. Källhammer, H. Pettersson, G. Stemme, Uncooled infrared bolometer arrays operating in a low to medium vacuum atmosphere: Performance model and tradeoffs. *Proc. SPIE* **6542**, 65421M (2007).
51. R. Shi, N. Shen, J. W. Wang, W. J. Wang, A. Amini, N. Wang, C. Cheng, Recent advances in fabrication strategies, phase transition modulation, and advanced applications of vanadium dioxide. *Appl. Phys. Rev.* **6**, 011312 (2019).
52. A. Khandelwal, N. Athreya, M. Q. Tu, L. L. Janavicius, Z. Yang, O. Milenkovic, J. P. Leburton, C. M. Schroeder, X. Li, Self-assembled microtubular electrodes for on-chip low-voltage electrophoretic manipulation of charged particles and macromolecules. *Microsyst. Nanoeng.* **8**, 27 (2022).
53. A. Khandelwal, Z. Ren, S. Namiki, Z. Yang, N. Choudhary, C. Li, P. Wang, Z. Mi, X. Li, Self-rolled-up aluminum nitride-based 3D architectures enabled by record-high differential stress. *ACS Appl. Mater. Interfaces* **14**, 29014–29024 (2022).
54. I. S. Chun, V. B. Verma, V. C. Elarde, S. W. Kim, J. M. Zuo, J. J. Coleman, X. Li, InGaAs/GaAs 3D architecture formation by strain-induced self-rolling with lithographically defined rectangular stripe arrays. *J. Cryst. Growth* **310**, 2353–2358 (2008).
55. Q. Zhong, Z. Tian, M. H. Dastjerdi, Z. Mi, D. V. Plant, Characterization of azimuthal and longitudinal modes in rolled-up InGaAs/GaAs microtubes at telecom wavelengths. *Opt. Express* **21**, 18909–18918 (2013).
56. W. Huang, J. Zhou, P. J. Froeter, K. Walsh, S. Liu, M. D. Kraman, M. Li, J. A. Michaels, D. J. Sievers, S. Gong, X. Li, Three-dimensional radio-frequency transformers based on a self-rolled-up membrane platform. *Nat. Electron.* **1**, 305–313 (2018).
57. W. Huang, X. Yu, P. Froeter, R. Xu, P. Ferreira, X. Li, On-chip inductors with self-rolled-up SiN_x nanomembrane tubes: A novel design platform for extreme miniaturization. *Nano Lett.* **12**, 6283–6288 (2012).
58. T. Deng, Z. H. Zhang, Y. X. Liu, Y. X. Wang, F. Su, S. S. Li, Y. Zhang, H. Li, H. J. Chen, Z. R. Zhao, Y. Li, Z. W. Liu, Three-dimensional graphene field-effect transistors as high-performance photodetectors. *Nano Lett.* **19**, 1494–1503 (2019).

59. Y. Guo, B. Peng, R. Qiu, G. Dong, Y. Yao, Y. Zhao, Z. Zhou, M. Liu, Self-rolling-up enabled ultrahigh-density information storage in freestanding single-crystalline ferroic oxide films. *Adv. Funct. Mater.* **33**, 2213668 (2023).
60. B. Zhao, Z. Wan, Y. Liu, J. Q. Xu, X. D. Yang, D. Y. Shen, Z. C. Zhang, C. H. Guo, Q. Qian, J. Li, R. X. Wu, Z. Y. Lin, X. X. Yan, B. L. Li, Z. W. Zhang, H. F. Ma, B. Li, X. Chen, Y. Qiao, I. Shakir, Z. Almutairi, F. Wei, Y. Zhang, X. Q. Pan, Y. Huang, Y. Ping, X. D. Duan, X. F. Duan, High-order superlattices by rolling up van der Waals heterostructures. *Nature* **591**, 385–390 (2021).
61. Q. L. Guo, G. Wang, D. Chen, G. J. Li, G. S. Huang, M. Zhang, X. Wang, Y. F. Mei, Z. F. Di, Exceptional transport property in a rolled-up germanium tube. *Appl. Phys. Lett.* **110**, 112104 (2017).
62. C. Chen, C. Li, S. Min, Q. Guo, Z. Xia, D. Liu, Z. Ma, F. Xia, Ultrafast silicon nanomembrane microbolometer for long-wavelength infrared light detection. *Nano Lett.* **21**, 8385–8392 (2021).

Acknowledgments: Part of the sample fabrication was performed at Fudan Nano-fabrication Laboratory. **Funding:** This work is supported by the National Key Technologies R&D Program of China (2021YFE0191800 to Y.M. and 2021YFA0715302 to G.H.), the National Natural Science Foundation of China (61975035 to Y.M.), and the Science and Technology Commission of Shanghai Municipality (22ZR1405000 to G.H.). **Author contributions:** Y.M. conceived the idea for the project and designed the experiments. B.W., B.C., and C.L. fabricated the devices and performed the electronic and optoelectronic measurements. Z.Zhang and B.W. performed thermal and optical simulation. B.W., Z.Zheng, and X.L. performed the TEM experiments and analyzed the data. J.W., Y.W., and B.W. performed the Raman experiments. B.W. and C.Y. performed the absorbance measurements. B.W., G.H., and Y.M. cowrote the manuscript. All authors discussed the results and commented on the manuscript. **Competing interests:** The authors declare that they have no competing interests. **Data and materials availability:** All data needed to evaluate the conclusions in the paper are present in the paper and/or the Supplementary Materials.

Submitted 21 May 2023
Accepted 15 September 2023
Published 18 October 2023
10.1126/sciadv.adi7805

ScienceAdvances

One-step rolling fabrication of VO_2 tubular bolometers with polarization-sensitive and omnidirectional detection

Binmin Wu, Ziyu Zhang, Bingxin Chen, Zhi Zheng, Chunyu You, Chang Liu, Xing Li, Jinlong Wang, Yunqi Wang, Enming Song, Jizhai Cui, Zhenghua An, Gaoshan Huang, and Yongfeng Mei

Sci. Adv. **9** (42), eadi7805. DOI: 10.1126/sciadv.adi7805

Science Advances (ISSN 2375-2548) is published by the American Association for the Advancement of Science. 1200 New York Avenue NW, Washington, DC 20005. The title *Science Advances* is a registered trademark of AAAS.